Identification of Active Sites for Ammonia Electrosynthesis on Ruthenium

Lin Hu,[1†] Hemanth Somarajan Pillai,[2†] Corbin Feit,[1†] Kaige Shi,[3] Zhengning Gao,[1] Parag Banerjee,[1,4,5,6*] Hongliang Xin,[2*] Xiaofeng Feng[1,3,4,5,7*]

[1]Department of Materials Science and Engineering, University of Central Florida, Orlando, Florida 32816, United States

[2]Department of Chemical Engineering, Virginia Polytechnic Institute and State University, Blacksburg, Virginia 24061, United States

[3]Department of Physics, University of Central Florida, Orlando, Florida 32816, United States

[4]Renewable Energy and Chemical Transformations (REACT) Cluster, University of Central Florida, Orlando, Florida 32816, United States

[5]NanoScience and Technology Center, University of Central Florida, Orlando, Florida 32816, United States

[6]Florida Solar Energy Center, University of Central Florida, Orlando, Florida 32816, United States

[7]Department of Chemistry, University of Central Florida, Orlando, Florida 32816, United States

[†]These authors contributed equally to this work.

*Email: Parag.Banerjee@ucf.edu (P.B.); hxin@vt.edu (H.X.); Xiaofeng.Feng@ucf.edu (X.F.)

Abstract:

Electrochemical N_2 reduction reaction (NRR) provides an attractive approach towards sustainable NH_3 production, while the design of electrocatalysts for NRR is hindered by the lack of knowledge on the structure-activity relationships and active sites. Here we report a prominent size-dependent activity for the NRR on Ru nanoparticles prepared by atomic layer deposition. As the Ru particle size increased from 2.1 to 8.4 nm, the mass activity and Faradaic efficiency for NH_3 production both decreased monotonically, while the specific (Ru-surface-area-normalized) activity reached the highest value on 3.8-nm Ru nanoparticles but declined by 5-fold on 8.4-nm Ru nanoparticles. Density functional theory (DFT) calculations and free energy analysis of elementary steps revealed the Ru D_5 step site, with its maximal population at ~4 nm particles, as the active site for the NRR on Ru, because it favors the adsorption of the $*N_2H$ intermediate compared to other surface sites while not getting poisoned by the $*NH_2$ intermediate.

Table of Contents (TOC) Graphic:

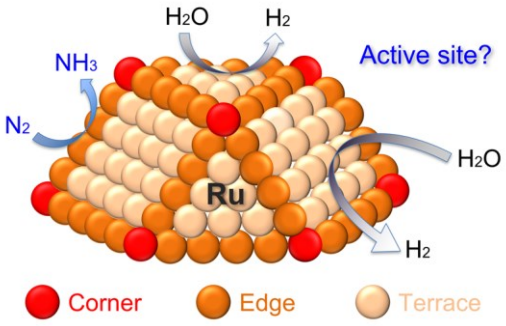

The industrial production of chemicals and fuels has mainly relied on fossil feedstocks, which however have limited reserves and are causing environmental problems. Thus, there is a growing demand for renewable energy technologies that can produce chemicals and fuels using solar and wind energy. One important example is the production of ammonia (NH_3), a key ingredient in agricultural fertilizers, via the Haber-Bosch process at high temperature and high pressure, which is energy-intensive and consumes 3−5% of the world's natural gas output.[1] Therefore, numerous efforts have been devoted to developing technologies and processes for the sustainable production of NH_3.[2] In particular, the electrochemical reduction of N_2 to NH_3 under ambient conditions has recently received considerable interest, because it is compatible with the intermittent renewable energy supplies such as solar- or wind-generated electricity and has the potential for sustainable, distributed production of NH_3.[3,4]

The development of an NH_3 electrosynthesis process has been hindered by the lack of efficient electrocatalysts for the N_2 reduction reaction (NRR): $N_2 + 8H^+ + 6e^- \rightarrow 2NH_4^+$ (product is in the form of aqueous NH_4^+ in neutral electrolyte).[5−7] The NRR is thermodynamically favorable with a standard potential of 0.274 V vs the normal hydrogen electrode,[8] but it suffers from sluggish kinetics due to the barrier of N_2 activation and the competition of the H_2 evolution reaction (HER).[6] It is generally agreed that the NRR at ambient conditions occurs via an associative mechanism,[3] where N≡N bond breaks after partial hydrogenation of N_2 molecules adsorbed on a catalyst surface. In such a mechanism, the reaction rate is considered to be limited by the first hydrogenation step of N_2 molecules adsorbed on catalyst surfaces.[5] Another major challenge for NH_3 electrosynthesis is the low selectivity (Faradaic efficiency) due to the competition of the HER, which is kinetically more favorable and occupies the vast majority of electrons and protons at the electrode-electrolyte interface, leading to a low Faradaic efficiency for NH_3 production.[6]

To date, numerous catalytic materials have been tested for the NRR, including noble metals such as Ru, Pt, Au, and Pd,[9−19] non-noble metals such as Fe, Ni, Mo, and Bi, and their oxides,[20−23] metal nitrides,[24,25] carbon-based materials,[26,27] and Li-mediated method.[28,29] Due to the low yield of NH_3 in typical NRR studies, the quantification of produced NH_3 often relies on the indophenol blue method,[30] which however may be interfered by unnoticed N-containing contaminations from the environment such as electrode, electrolyte, and cell.[31−33] Accordingly, rigorous protocols for validating and quantifying NH_3 production have been proposed to improve the reliability of NRR performance data.[34−38] In addition, the NH_3 production rates are often reported in the form of mass activity (normalized to catalyst mass), making it difficult to compare and understand the intrinsic activity of a catalyst, as various particle sizes, shapes, and loadings are used in different studies. Therefore, we suggest that the electrochemical surface area (ECSA) of a catalyst material should be measured, so that specific (surface-area-normalized) activity or turnover frequency for the NRR can be determined and compared to understand the catalyst's intrinsic activity.[35,39]

A rational design of catalysts for the NRR relies on our understanding of catalytic active sites and structure-activity relationships.[7] For metal nanocatalysts, many efforts are focused on tuning structural parameters such as particle size, shape, composition, and defects. Such efforts played an important role in the development of metal nanocatalysts for CO_2 electroreduction. For example, Pd and Au nanoparticles with different sizes were prepared and evaluated for CO_2 reduction, which showed different activities and Faradaic efficiencies due to the size-dependent population of low-coordinated surface sites such as corner, edge, and terrace sites. These sites have different binding energies with reaction intermediates such as *COOH and *H and thus different activities for CO_2 reduction and HER, which explains the size-dependent catalytic performance for CO_2 reduction.[40] Therefore, understanding the particle size effect can help identify active sites and design efficient catalysts by controlling surface atomic arrangement. Such studies and corresponding insights into the active sites for the NRR are still lacking.[41]

Here, we investigate the active sites for the NRR on Ru by studying its particle size effect in the NRR catalysis. We use Ru as a model catalyst in this work because it is one of the most active catalysts for the NRR due to its optimal binding strength with reaction intermediates.[5,9] Despite the reports of NH_3 production on various Ru-based catalysts,[10–16] understanding of the active sites for NRR is still limited. To tackle this challenge, we prepared Ru nanoparticles with controlled sizes ranging from 2.1 to 8.4 nm using atomic layer deposition (ALD) and compared their catalytic performance for the NRR. As a result, the mass activity, specific (surface-area-normalized) activity, and Faradaic efficiency for NH_3 production all showed a strong dependence on Ru particle size. Particularly, the specific activity reached the highest value for 3.8-nm Ru particles but declined by 5-fold as the particle size increased to 8.4 nm, showing a critical effect of Ru particle size. Density functional theory (DFT) calculations and free energy analysis of elementary steps revealed the Ru D_5 step site as the active site for the NRR, and a maximal population of such site at ~4 nm particles agrees well with the size dependence of the NRR activity on Ru nanoparticles.

We first tried a polyol reduction method to prepare Ru nanoparticles with controlled sizes.[42] Figure 1a shows a typical TEM image of the derived Ru nanoparticles dispersed on carbon black (Ru/C), and particle size statistics gave an average size of 2.5 ± 0.9 nm (Figure S1). As the particle size was not very uniform, we further added polyvinylpyrrolidone (PVP) as a surfactant in the synthesis process to control the particle size (see Experimental Methods in the Supporting Information).[43] Consequently, the obtained Ru(PVP)/C nanoparticles were more uniform in size (2.0 ± 0.3 nm), as shown by the TEM image in Figure S1, confirming the effect of PVP surfactant. However, PVP binds strongly to metals and may not be completely removed from Ru surface even after cleaning treatments.[43,44] Although the residual PVP contains nitrogen and might cause false positive in NH_3 quantification, in fact, the Ru(PVP)/C catalyst showed a much lower yield of NH_3 than the Ru/C catalyst under identical NRR test conditions (Figure S1). Therefore, we postulate that the residual PVP may bind to those Ru surface sites with a stronger binding affinity, such as

step sites, which blocked those Ru surface sites from N_2 adsorption and reduction.[43,44] Thus, the Ru(PVP)/C sample was not used in the following study.

ALD was then introduced to prepare size-controlled Ru nanoparticles without surfactant, as ALD can enable a monolayer control of the growth of nanoparticles. Particularly, we deposited Ru nanoparticles on an AvCarb GDS2230 substrate, which has a hydrophobic coating layer and may cause difficulty in the nucleation of Ru that is a water-based chemistry. Thus, clusters of Ru nuclei germinate initially. As the ALD cycle numbers increase, these clusters can grow and eventually merge as a polycrystalline film. For example, on a Si substrate with native oxide (i.e., hydrophilic) the film formation usually begins at ≥ 40 ALD cycles, as previously reported.[45] Since the formation of Ru nanoparticles is critical for catalyst activity, the number of ALD cycles was controlled. For a hydrophobic substrate such as the AvCarb GDS2230, the number of ALD cycles was kept ≤ 80. As will be seen below, this approach was adequate to provide discrete and precise tunability of the Ru nanoparticle size. Thus, the ability of ALD to deposit on incompatible surfaces is exploited to create precisely tuned Ru nuclei with controllable size and size distribution.

To examine the morphology of the ALD-Ru samples, SEM images were acquired for a carbon substrate before and after deposition, as shown in Figure S2, where the deposited Ru nanoparticles were readily visible on the substrate. TEM characterization was performed to further investigate the Ru nanoparticles in the samples. Figure 1b-e showed typical TEM images of Ru nanoparticles that were uniformly deposited on the substrate by ALD with a targeted size of 2, 4, 6, and 8 nm, respectively, which are hereafter referred as ALD-Ru-2, ALD-Ru-4, ALD-Ru-6, and ALD-Ru-8 samples. The ALD Ru nanoparticles were similar in shape, and their actual size distributions were found to be 2.1 ± 0.4, 3.8 ± 0.6, 5.9 ± 0.8, and 8.4 ± 1.1 nm, respectively, as presented in Figure S3 and Table 1, which were derived by measuring over 200 particles in the TEM images of each sample. A representative high-resolution TEM image of the Ru nanoparticles was shown in Figure 1f, where the spacing of the lattice fringes was determined to be 0.210 nm, corresponding to the $(10\bar{1}1)$ crystal planes of Ru. Therefore, a series of size-controlled Ru nanoparticle samples were prepared by ALD, ranging from 2.1 to 8.4 nm with narrow size distributions.

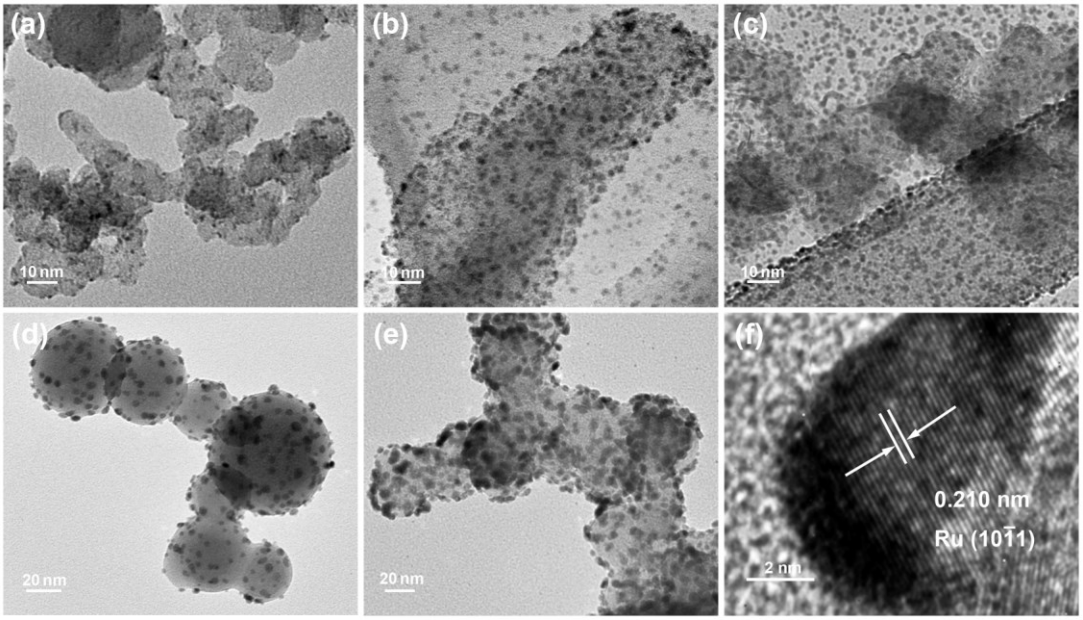

Figure 1. TEM images of Ru nanoparticle samples. (a) Ru/C sample prepared by polyol reduction method. (b-e) ALD-Ru samples with a targeted size of (b) 2, (c) 4, (d) 6, and (e) 8 nm, referred as ALD-Ru-2, ALD-Ru-4, ALD-Ru-6, and ALD-Ru-8 samples. (f) High-resolution TEM image of a Ru nanoparticle, showing lattice fringes with a spacing of 0.210 nm.

Table 1. Summary of the Ru nanoparticles on carbon substrate (1 × 1 cm^2) prepared by polyol reduction and ALD, respectively.

Sample	Ru/C	ALD-Ru-2	ALD-Ru-3	ALD-Ru-4	ALD-Ru-6	ALD-Ru-8
Particle Size (nm)	2.5 ± 0.9	2.1 ± 0.4	3.3 ± 0.6	3.8 ± 0.6	5.9 ± 0.8	8.4 ± 1.1
ECSA of Ru (cm^2)	4.3 ± 0.5	1.9 ± 0.2	2.2 ± 0.2	3.0 ± 0.2	6.0 ± 0.7	12.8 ± 1.6
Ru Loading (mg)	0.20 ± 0.02	0.06 ± 0.01	0.09 ± 0.03	0.16 ± 0.04	0.55 ± 0.03	1.86 ± 0.16

In addition, X-ray diffraction (XRD) and X-ray photoelectron spectroscopy (XPS) were used to examine the structure and chemical state of the ALD-Ru samples. Figure 2a shows the grazing-incidence XRD patterns of the ALD-Ru samples, with peaks from Ru as well as two characteristic peaks of graphitic carbon in the substrate. By comparing to the standard powder diffraction file of hexagonal Ru (JCPDS No. 06-663), the XRD peaks of Ru were identified as the (0002), (10$\bar{1}$1), and (10$\bar{1}$3) planes of metallic Ru, as labelled in Figure 2a. The diffraction peaks of Ru showed a relatively lower intensity compared to that of carbon due to the small loading of Ru on the carbon substrate. Figure 2b shows the XPS spectra of the ALD-Ru samples, indicating the presence of Ru,

C, and O in the samples, where the C and O were attributed to the carbon substrate. It should be noted that the Ru 3d peak (284 eV for $3d_{3/2}$ and 280 eV for $3d_{5/2}$) overlaps with the C 1s peak (284 eV), so we use the Ru 3p peaks to identity the chemical state. The intensity of Ru 3p doublet peaks increased along with the increase of deposited Ru particle size, while the binding energies of Ru $3p_{1/2}$ and $3p_{3/2}$ peaks were the same for all ALD-Ru samples and were found to be 484.4 and 462.1 eV, respectively, which are concordant with the binding energy values of Ru metals and confirm the metallic state of the ALD-Ru particles. Additionally, no N 1s peak at ~400 eV was observed within the detection limit of the XPS for the ALD-Ru samples.

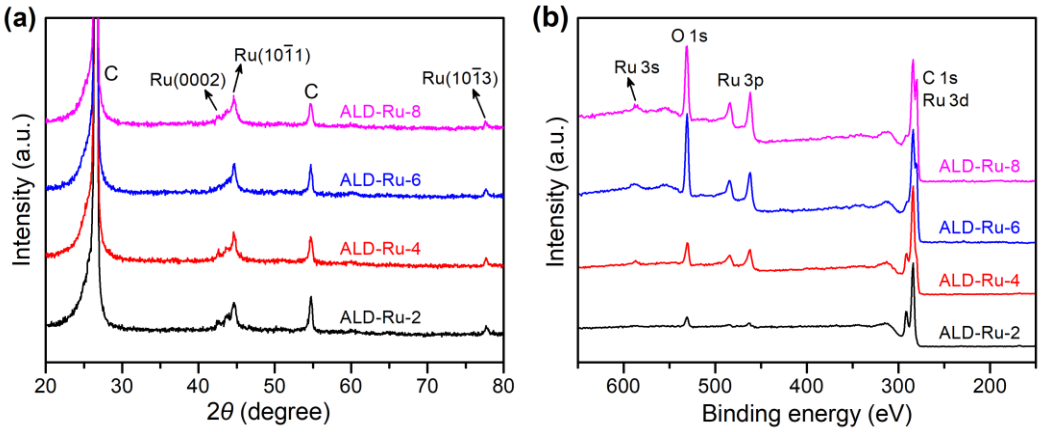

Figure 2. Characterization of the ALD-Ru samples. (a) Grazing-incidence XRD patterns of the ALD-Ru samples, with the XRD peaks labelled for Ru and carbon. (b) XPS spectra of the ALD-Ru samples.

As indicated above, it is necessary to measure the ECSA of Ru in each electrode, so that the specific (surface-area-normalized) activity for the NRR can be determined to reveal structure-activity relationships. Here we quantified the ECSA of Ru by the underpotential deposition (UPD) of Cu on Ru surface. For each electrode, cyclic voltammetry (CV) scans were first performed in a 0.1 M H_2SO_4 electrolyte, and then in an electrolyte containing 0.1 M H_2SO_4 and 0.5 mM $CuSO_4$, where the Cu UPD and stripping peaks can be easily identified.[46] The CV scans were carried out from 0.05 to 0.95 V vs RHE at a scan rate of 10 mV s^{-1}, and the anodic peak at around 0.4−0.5 V vs RHE was attributed to the stripping of underpotential deposited Cu from Ru surface, as shown in Figure S4. The charges associated with Cu stripping were determined by integrating the peak area in the CV curves, which were converted to ECSA using a conversion factor of 420 μC cm^{-2}.[46] The ECSA of Ru measured for all electrodes was summarized in Table 1.

The Ru electrodes were evaluated for the NRR in 0.1 M $LiClO_4$ electrolyte using a gas-tight two-compartment electrochemical cell (H-cell), as shown in Figure S5. $LiClO_4$ electrolyte was selected for the NRR, as a neutral electrolyte can suppress the HER compared to acidic or alkaline electrolytes and can thus benefit the NRR.[19] In addition, Li^+ ions may facilitate the adsorption of

N_2 to enhance the NRR.[47] The produced NH_3 was quantified by the indophenol blue method using the established calibration curves in Figure S6.[30] Another possible product hydrazine (N_2H_4) was also examined using a spectrophotometric method based on the calibration curves in Figure S7,[48] while no N_2H_4 was detected in this work. Before the study of NRR activities, we quantitatively determined the background levels of NH_3 and NO_x (both gaseous and ionic NO_x compounds) in the N_2 gas and the electrolyte, and then purified them if possible. These N-contaminants can be simultaneously reduced to NH_3 along with the NRR, which may cause false positive results for NH_3 production.[38] First, we quantified the level of NH_3 and gaseous NO_x in the N_2 gas via the following steps: (1) N_2 gas was passed through an acid trap (0.05 M H_2SO_4 solution) to capture NH_3 in the gas; (2) the gas was passed through $KMnO_4$ solution (so that NO was converted to more soluble NO_2) and then through 0.1 M KOH solution, in which NO_2 gas molecules were absorbed and rapidly transformed to NO_2^- and NO_3^- ions in the solution,[49] as shown in Figure S9a. The N_2 gas flow rate and time (5 sccm, 1 h) were the same as the NRR test conditions. The NH_3 captured in the first step, and the NO_x captured in the second step were quantified by the indophenol blue method and the Griess method (see Figure S8 in the Supporting Information),[50] respectively. As a result, the levels of NH_3 and NO_x captured from the N_2 gas were at least 40 times lower than that detected in a typical NRR test, as shown in Figure S9b. Similarly, we performed the same evaluation for the purified $^{15}N_2$ gas and obtained similar results, as shown in Figure S9c-d. Thus, the background levels of N-contaminants in the N_2 gas should not impact the NRR results. Nevertheless, we used this trap system to purify the N_2 gas for the NRR studies, as shown in Figure S9a and S9c, so that the N-contaminants in the N_2 gas can be further eliminated. For the possible ionic NO_x compounds (NO_2^- and NO_3^- ions) in the electrolyte, we cannot directly remove them from the electrolyte, so we used an electrolysis with Ru catalyst at −0.10 V vs RHE under Ar gas flow to convert them to NH_4^+, as Ru is a highly active catalyst for the electroreduction of NO_2^- and NO_3^- ions.[51] After the Ar control test, the levels of NH_4^+ and NO_2^- were found to be at least 50 times lower than that detected in typical NRR test, as shown in Figure S9e-f. Therefore, the possible influence of N-contaminants from the N_2 gas and electrolyte can be excluded, and the N_2 gas was further purified using the trap system for the study of NRR.

Moreover, we confirmed the N source of the detected NH_3 by additional control experiments and ^{15}N isotopic labeling experiment. Control experiments without Ru catalyst or with Ar feeding gas were carried out under otherwise identical conditions. As shown in Figure 3a, no apparent NH_3 was detected by the indophenol blue method for the substrate without Ru loading or when Ar gas was bubbled into the electrolyte, indicating that NH_3 could only be produced with the presence of Ru catalyst and N_2 feeding gas. Additionally, ^{15}N isotopic labeling experiment was performed to verify the N source of the detected NH_3. When the purified $^{15}N_2$ gas (see Experimental Methods in the Supporting Information) was fed into the NRR test, only $^{15}NH_4^+$ with a doublet feature was observed in the ^1H nuclear magnetic resonance (NMR) spectrum of the post-reaction electrolyte,

as exhibited in Figure 3b. Consistently, only $^{14}NH_4^+$ with a triplet feature was observed in the NMR spectrum when $^{14}N_2$ gas was fed into the electrolysis, and no NH_4^+ was found when Ar gas was supplied. Therefore, both experiments confirmed that NH_3 was only produced when N_2 gas and Ru catalyst were present. We can now conclude that the detected NH_3 is truly produced from the Ru-catalyzed electroreduction of N_2 gas.

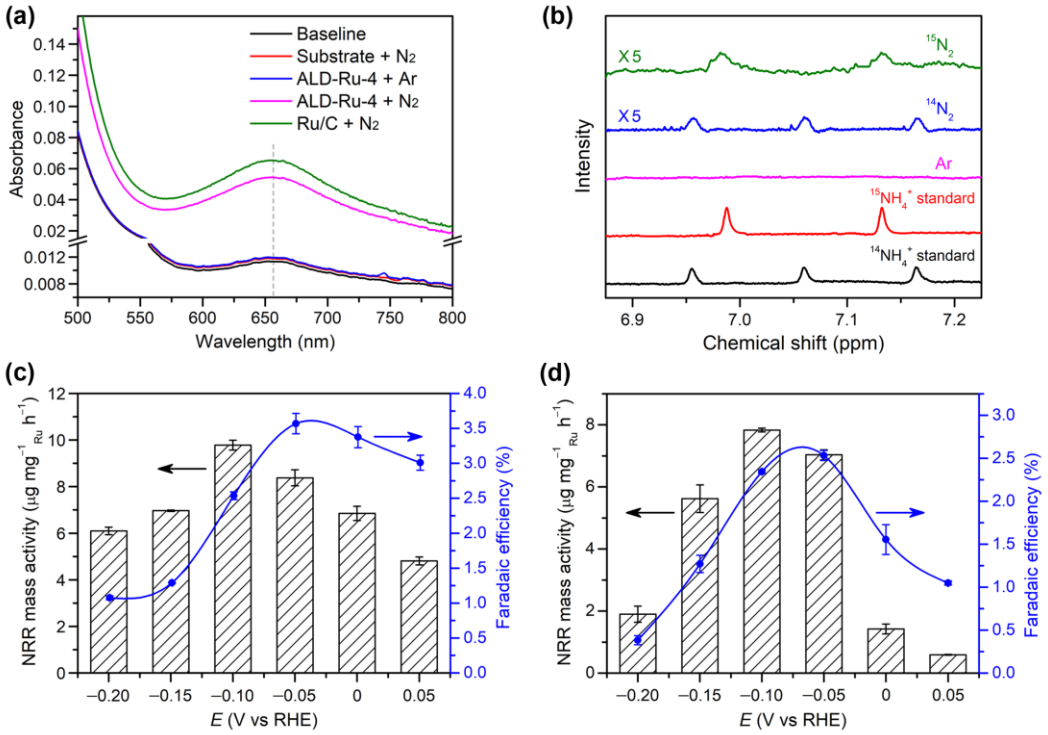

Figure 3. Evaluation of the NRR catalytic performance on Ru samples. (a) Representative UV-vis absorption spectra of the post-reaction electrolytes after NRR test at −0.10 V vs RHE for 1 h under different conditions. No apparent NH_3 was detected for the tests without Ru catalyst or with Ar feeding gas. (b) ^1H NMR spectra obtained for the post-reaction electrolytes after electrolysis with $^{15}N_2$, $^{14}N_2$, and Ar feeding gases, respectively. (c-d) Mass activity and Faradaic efficiency for the NRR on the (c) Ru/C and (d) ALD-Ru-4 samples in 0.1 M $LiClO_4$ electrolyte at various potentials. The error bars represent standard deviations of measurements on three independently prepared samples.

Based on the above rigorous analysis of the N source of detected NH_3, we can now investigate and quantitatively compare the NRR activity. We first examined the potential dependence of the NRR activity on the Ru/C and ALD-Ru-4 (as a representative ALD sample) samples to understand the NRR electrokinetics and identify an appropriate potential for the comparison of NRR activity among the samples. As the potential shifted from 0.05 to −0.20 V vs RHE, the total current density on the Ru/C electrode increased from 0.13 to 0.80 mA cm^{-2}, as shown by the chronoamperometric

curves in Figure S10a. The mass activity for the NRR was determined to be 4.8 μg mg^{-1}_{Ru} h^{-1} at 0.05 V, which increased to a maximum value of 9.8 μg mg^{-1}_{Ru} h^{-1} at −0.10 V, but declined to 6.1 μg mg^{-1}_{Ru} h^{-1} at −0.20 V, as shown in Figure 3c. The Faradaic efficiency for NH_3 production had a similar trend, which increased from 3.0% to 3.6% as the potential shifted from 0.05 to −0.05 V but declined rapidly to 1.1% at −0.20 V due to the higher total current density. Similar potential dependence was observed on the ALD-Ru-4 sample: the total current density increased from 0.04 to 0.67 mA cm^{-2} as the potential shifted from 0.05 to −0.20 V vs RHE (chronoamperometric curves in Figure S10b), while a maximum mass activity of 7.8 μg mg^{-1}_{Ru} h^{-1} was reached at −0.10 V and a highest Faradaic efficiency of 2.5% was observed at −0.05 V (Figure 3d).

The NRR activity on the two Ru samples showed a similar potential dependence, indicating a general electrokinetic behavior of the NRR catalysis: the activity first increases as the overpotential rises until a maximum value is reached, but then declines at further increased overpotentials. Such an electrokinetic behavior was generally observed for the NRR on other catalytic materials.[17,20–23] As the NRR has not reached the mass transport limitation yet, the decline of the NRR activity at relatively higher overpotentials is attributed to the competition of the HER.[39] The activity of the HER increases exponentially with the overpotential, leading to a higher coverage of *H on Ru surface and consequently fewer surface sites available for the adsorption of $*N_2$, which has a weak binding strength and can be easily influenced by competing adsorption species. Thus, the highest activity for the NRR on Ru is reached at −0.10 V, so we will compare the NRR activities of all Ru samples at this potential, which can represent their catalytic performance for the NRR.

Subsequently, all Ru samples were evaluated for the NRR at −0.10 V vs RHE in 0.1 M $LiClO_4$ electrolyte. The mass activity, specific activity, and Faradaic efficiency for NH_3 production on the Ru samples were determined and compared to understand the Ru particle size effect. As shown in Figure 4a, the NRR mass activity decreased monotonically from 12.1 to 0.65 μg mg^{-1}_{Ru} h^{-1} as the particle size increased from 2.1 to 8.4 nm. This is mainly due to the surface-area-to-mass ratio: the smaller the particle is, the larger the Ru surface area per unit mass is for catalyzing the NRR. In contrast, the NRR specific activity showed a different dependence on the Ru particle size: it first increased from 0.44 to 0.57 μg cm^{-2}_{Ru} h^{-1} as the particle size increased from 2.1 to 3.8 nm, but declined significantly to 0.11 μg cm^{-2}_{Ru} h^{-1} as the particle size further increased to 8.4 nm, as shown in Figure 4b. Accordingly, the 3.8-nm particles showed the highest specific activity for the NRR, so they should have the largest population of active sites for the NRR. The 5-fold decline of the specific activity from 3.8 to 8.4 nm indicated that the size-dependent population of surface sites had a major impact on the NRR catalysis, which will be discussed later. Interestingly, the data point of the Ru/C sample in Figure 4a-b showed a good consistency with the trend of the ALD-Ru sample data, further confirming the reliability of our NRR data measured over samples prepared by different methods.

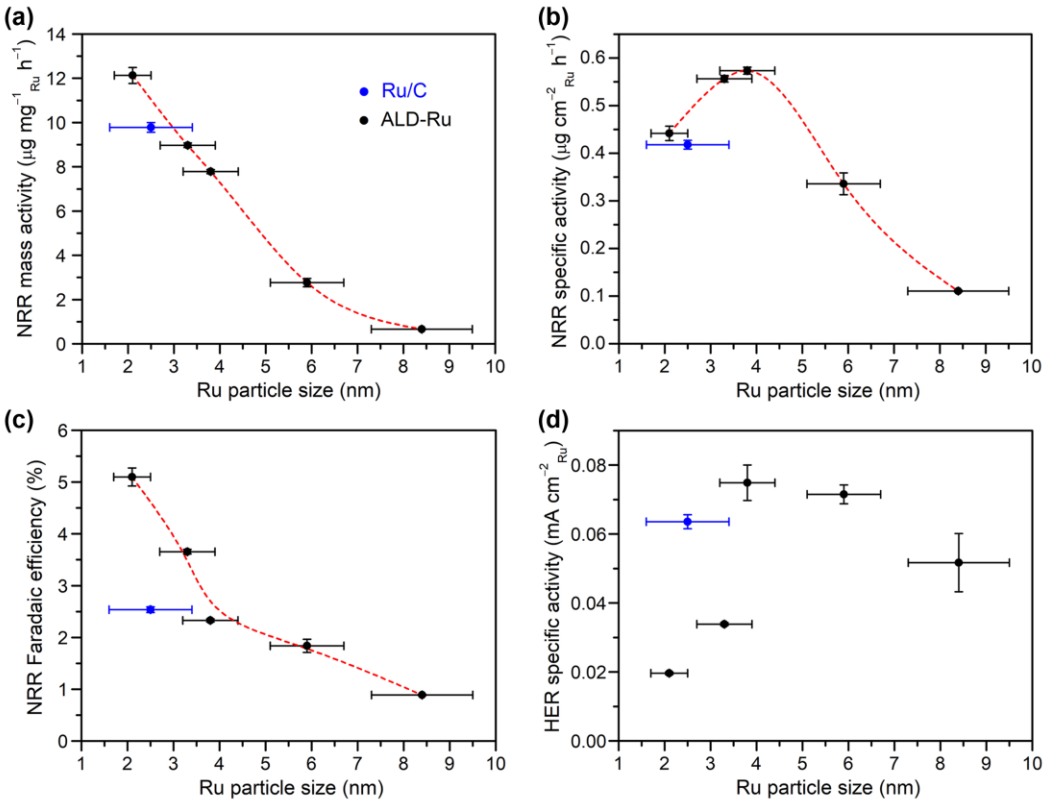

Figure 4. Dependence of the (a) NRR mass activity, (b) NRR specific activity, (c) NRR Faradaic efficiency, and (d) HER specific activity on the Ru nanoparticle size during the NRR electrolysis. The horizontal error bars represent standard deviations of Ru nanoparticle sizes, and the vertical error bars represent standard deviations of measurements on three independently prepared samples.

Similar to the size dependence of the mass activity, the Faradaic efficiency for NH_3 production on the ALD-Ru samples decreased monotonically from 5.1% to 0.9% as the particle size increased from 2.1 to 8.4 nm, as exhibited in Figure 4c. The Ru/C sample showed a Faradaic efficiency of 2.5%, which is around half that of the ALD-Ru-2 sample (5.1%). As the Faradaic efficiency is determined by the competition between the NRR and HER, we derived the specific activity for the HER in the electrolysis, as shown in Figure 4d. The HER specific activity was largely similar on the Ru/C, ALD-Ru-4, ALD-Ru-6, and ALD-Ru-8 samples, but was lower on the ALD-Ru-2 and ALD-Ru-3 samples. This is different from our expectation, as smaller Ru nanoparticles may have more low-coordinated surface sites that boost the HER.[40] We attributed the lower HER activity on the two samples to the exposed hydrophobic surface of the AvCarb GDS2230 substrate with small Ru nanoparticles. To verify this hypothesis, we tested the NRR on an ALD-Ru-2 sample deposited on an AvCarb MGL370 substrate that is less hydrophobic. Figure S11a showed the configurations of the two electrodes, and their difference in hydrophobicity was confirmed by the contact angle measurements in Figure S11b. Under the same NRR test conditions, the GDS2230 electrode had

a total current density of ~0.05 mA cm^{-2}, which is around one order of magnitude lower than that of the MGL370 electrode (>0.5 mA cm^{-2}), as exhibited in Figure S11c. Interestingly, the two electrodes showed similar NRR activities (13.5 vs 12.1 μg mg^{-1}_{Ru} h^{-1}), but the Faradaic efficiency was distinct: 0.84% for the MGL370 electrode and 5.1% for the GDS2230 electrode, as shown in Figure S11d, due to the lower total current density and suppressed HER activity on the GDS2230 substrate. This explains the lower HER activity on the ALD-Ru-2 sample, and also suggests that the electrode hydrophobicity can be employed to improve the NRR Faradaic efficiency.[39]

We further evaluated the stability of the ALD-Ru catalysts for the NRR electrolysis. As shown in Figure S12, the stability was assessed by consecutive recycling electrolysis on the same ALD-Ru-4 electrode at −0.10 V vs RHE in N_2-saturated 0.1 M $LiClO_4$ electrolyte (1 hour each cycle). Fresh electrolyte was used in each cycle, which can reduce the contact time of the electrolyte with ambient environment to minimize the possible adsorption of N-contaminants.[38] The electrolysis showed similar current densities in the five cycles, and the NH_3 yield rate and Faradaic efficiency for NH_3 production remained largely unchanged during the five cycles, indicating a good stability of the ALD-Ru catalyst for the NRR. TEM images of the Ru nanoparticles in the post-electrolysis electrode showed a similar morphology as those in the as-prepared sample, confirming the stability test result. This is likely due to the enhanced binding and immobilization of the Ru nanoparticles on the carbon substrate enabled by the ALD technique.

DFT calculations were performed to understand the nature of the active Ru sites for the NRR and structure-activity relationships. Figure 5a shows a schematic Wulff-like Ru nanoparticle with color-coded surface sites. There are two types of terrace sites (0001) and $(10\bar{1}1)$ along with three different 5-atom step sites formed between them, denoted by A_5, B_5, and D_5, respectively.[52] The (0001) surface is the close packed terrace for the hcp crystal structure and is most commonly used in computational studies of catalysis. The $(10\bar{1}1)$ terrace has a mix of both the three-fold hollow and four-fold hollow sites. The B_5 and D_5 steps have a similar orientation of the 5 atoms while the D_5 is on a kink (Figure 5b). The A_5 step has a larger distance between the top and bottom terraces compared to the B_5 and D_5 steps. As the particle size varies, the population or density of these terrace and step sites on the surface will change,[52] which can affect the catalytic activity.

Theoretical studies have shown that generally there are two possible rate-limiting steps in the NRR on metal surfaces, i.e., N_2 adsorption forming $*N_2H$ and $*NH_2$ desorption into NH_3 or NH_4^+.[5,9,53] Our DFT calculations suggest that the $*N_2$ adsorption favors an atop configuration with the molecular axis perpendicular to the surface. Due to a significant activation barrier (>0.6 eV) for $*N_2$ rotation on metal surfaces,[54] the proton-coupled electron transfer to $*N_2$ goes through a monodentate $*N_2H$ at the bridge site, followed by a more stable bidentate adsorption (Figure 5b). Hydrogenating the nitrogen atom of $*N_2H$ species in the distal or alternating pathways and the splitting of N-N bonds eventually lead to the formation of the $*NH_2$ intermediate, the desorption

of which results in the production of NH_3. DFT-calculated free formation energies of the monodentate $*N_2H$ and $*NH_2$ on surface bridge sites are linearly correlated, as shown in Figure S13. The linear adsorption-energy scaling naturally leads to a volcano-type relationship of the limiting potential using the free formation energy of $*NH_2$ as the reactivity descriptor. In contrast to previous studies, our free energy calculations with the consideration of a nearby *H and the low concentration of ammonium in the solution suggest that the adsorption of $*N_2H$ is the potential determining step on Ru surface, with the D_5 site near the optimum. The *H species facilitates the desorption of NH_3 while increasing the limiting potential of the first step.[9] It is also important to consider the activity of NH_4^+ in the solution,[19] which lowers the free energy change of the $*NH_2$ removal step. The (0001) terrace site has a largest generalized coordination number (7.33 for a bridge site) and lowest d-band center (−1.86 eV), which has a facile $*NH_2$ releasing step but limited by the weak adsorption of $*N_2H$ (~1.22 eV at 0 V vs RHE). The D_5 site strikes a perfect balance between the two limiting steps (Figure 5c) by possessing a unique local coordination environment, thus serving as the active site for the NRR. Although a recent study detected the accumulation of N=N species during the NRR on Ru,[11] suggesting N-N splitting as a possible rate-limiting step, our DFT calculations show that N-N splitting on various step sites are surmountable (Figure S14), consistent with a previous study.[9] Site population analysis of three step sites at Wulff-constructed Ru nanoparticles (Figure 5d) shows that a maximum population of the D_5 step site is reached on particles of ~4 nm in size,[52] which is in excellent agreement with the observed size dependence of the NRR specific activity on Ru nanoparticles. While a simplistic view was taken here, it captures the general trend of theoretical limiting potentials across metal sites. More rigorous models can be employed to investigate kinetic influence of the solvent, surface charging, and ionic distributions at the electrochemical interfaces.[55–58]

We also investigated HER at the Ru surface sites following the traditional Volmer-Heyrovsky mechanism. The differential free energy of adsorption for *H was calculated for the D_5 and $(10\bar{1}1)$ surfaces and we find it favorable for the formation of a complete monolayer of *H on both surfaces, as shown in Figure S15. The addition of the last *H on the D_5 step has a differential free formation energy close to 0 eV, whereas the differential free formation for the last *H on the $(10\bar{1}1)$ surface is −0.15 eV. This indicates that the D_5 step is more active for the HER than the $(10\bar{1}1)$ surface, suggesting a direct competition for active sites between the HER and the NRR and rationalizing a similar size dependence of the HER activity on Ru nanoparticles.

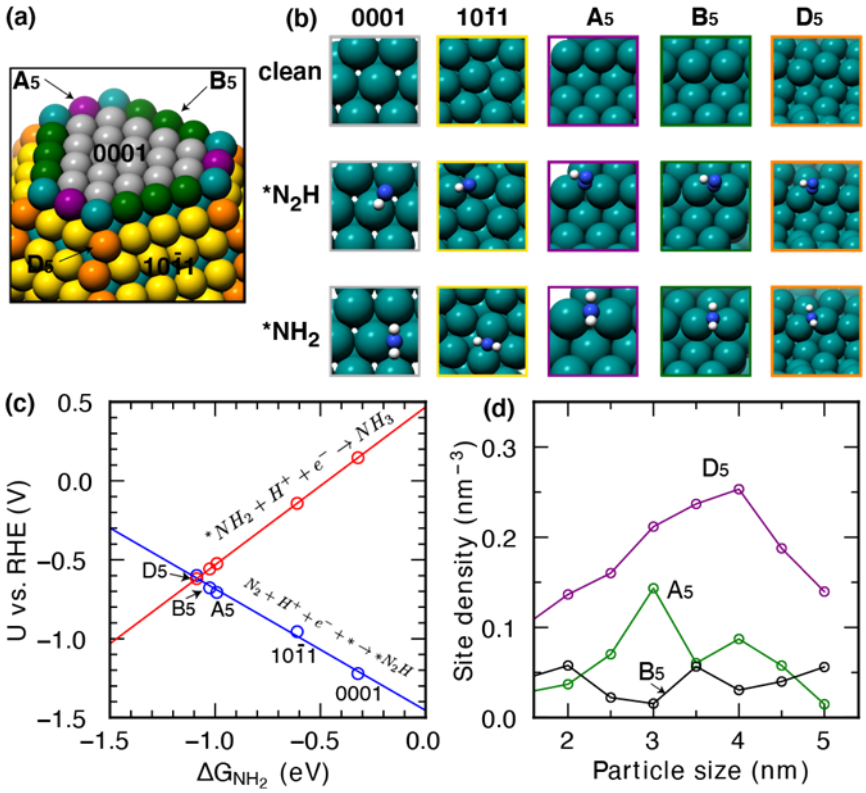

Figure 5. DFT calculations to identify the active sites for NRR. (a) A schematic Wulff-constructed Ru nanoparticle showing different terrace and step sites. (b) Geometric structures of clean, *N_2H, and *NH_2 at (0001), (10$\bar{1}$1), A_5, B_5, and D_5 sites (top view). (c) Theoretical limiting potentials for NRR as a function of the free formation energy of *NH_2 on different Ru surface sites. Two lines corresponding to the limiting potentials of the formation of *N_2H and the desorption of *NH_2 were derived from the scaling relations with 5 different sites denoted. (d) The density of different step sites as a function of Ru nanoparticle size. Adapted with permission from ref 52. Copyright 2008 by the American Physical Society.

In summary, we prepared size-controlled Ru nanoparticles by ALD and studied the effect of Ru nanoparticle size on the NRR to reveal the active sites. As the particle size increased from 2.1 to 8.4 nm, the mass activity for the NRR at −0.10 V vs RHE decreased monotonically from 12.1 to 0.65 μg mg^{-1}_{Ru} h^{-1}, with the corresponding Faradaic efficiency dropping from 5.1% to 0.9%. In contrast, the NRR specific activity reached the highest value for 3.8-nm particles but declined by 5-fold as the particle size increased to 8.4 nm, indicating a critical effect of the Ru particle size in the NRR catalysis. DFT calculations and free energy analysis of elementary steps revealed the D_5 step site as the active site for the NRR, because it favors the formation of the *N_2H intermediate compared to other step and terrace sites while not getting poisoned by the *NH_2 intermediate. The maximum population of the D_5 step site on the 4-nm Ru nanoparticles explains the size dependence of the NRR activity. Our study provides a fundamental understanding of the active sites for Ru-

catalyzed electrosynthesis of NH_3 as well as the structure-activity relationships for further catalyst design and optimization.

ASSOCIATED CONTENT

Supporting Information.

The Supporting Information is available free of charge at https://pubs.acs.org/doi/10.1021/acsenergylett.2c02175.

Experimental methods, additional materials characterization data, electrochemical data, and DFT calculation results (Figures S1−S15).

AUTHOR INFORMATION

Corresponding Authors

*Email: Parag.Banerjee@ucf.edu (P.B.); hxin@vt.edu (H.X.); Xiaofeng.Feng@ucf.edu (X.F.)

Author Contributions

†L.H., H.S.P., and C.F. contributed equally to this work.

ORCID

Xiaofeng Feng: 0000-0002-9473-2848

Hongliang Xin: 0000-0001-9344-1697

Notes

The authors declare no competing financial interest.

ACKNOWLEDGMENTS

This material is based upon work supported by the National Science Foundation under Grant No. 1943732. H.S.P and H.X. gratefully acknowledge the financial support of the NSF CAREER program (CBET-1845531). C.F. was supported by the National Science Foundation under Grant No. 1808625. The authors acknowledge the use of an XPS instrument supported by the NSF MRI: ECCS: 1726636. The computational resource used in this work is provided by the advanced research computing at Virginia Polytechnic Institute and State University.

REFERENCES

(1) Erisman, J. W.; Sutton, M. A.; Galloway, J.; Klimont, Z.; Winiwarter, W. How a century of ammonia synthesis changed the world. *Nat. Geosci.* **2008**, *1*, 636−639.

(2) Chen, J. G.; Crooks, R. M.; Seefeldt, L. C.; Bren, K. L.; Bullock, R. M.; Darensbourg, M. Y.; Holland, P. L.; Hoffman, B.; Janik, M. J.; Jones, A. K.; et al. Beyond fossil fuel–driven nitrogen transformations. *Science* **2018**, *360*, eaar6611.

(3) Shipman, M. A.; Symes, M. D. Recent progress towards the electrosynthesis of ammonia from sustainable resources. *Catal. Today* **2017**, *286*, 57−68.

(4) Qing, G.; Ghazfar, R.; Jackowski, S. T.; Habibzadeh, F.; Ashtiani, M. M.; Chen, C. P.; Smith III, M. R.; Hamann, T. W. Recent advances and challenges of electrocatalytic N_2 reduction to ammonia. *Chem. Rev.* **2020**, *120*, 5437−5516.

(5) Montoya, J. H.; Tsai, C.; Vojvodic, A.; Nørskov, J. K. The challenge of electrochemical ammonia synthesis: A new perspective on the role of nitrogen scaling relations. *ChemSusChem* **2015**, *8*, 2180−2186.

(6) Singh, A. R.; Rohr, B. A.; Schwalbe, J. A.; Cargnello, M.; Chan, K.; Jaramillo, T. F.; Chorkendorff, I.; Nørskov, J. K. Electrochemical ammonia synthesis—The selectivity challenge. *ACS Catal.* **2017**, *7*, 706−709.

(7) Guo, C.; Ran, J.; Vasileff, A.; Qiao, S. Z. Rational design of electrocatalysts and photo(electro)catalysts for nitrogen reduction to ammonia (NH_3) under ambient conditions. *Energy Environ. Sci.* **2018**, *11*, 45−56.

(8) Bard, A. J.; Parsons, R.; Jordan, J. Standard potentials in aqueous solution. Marcel Dekker: New York, **1985**; pp 138.

(9) Back, S.; Jung, Y. On the mechanism of electrochemical ammonia synthesis on the Ru catalyst. *Phys. Chem. Chem. Phys.* **2016**, *18*, 9161−9166.

(10) Wang, D.; Azofra, L. M.; Harb, M.; Cavallo, L.; Zhang, X.; Suryanto, B. H.; MacFarlane, D. R. Energy-efficient nitrogen reduction to ammonia at low overpotential in aqueous electrolyte under ambient conditions. *ChemSusChem* **2018**, *11*, 3416−3422.

(11) Yao, Y.; Wang, H.; Yuan, X. Z.; Li, H.; Shao, M. Electrochemical nitrogen reduction reaction on ruthenium. *ACS Energy Lett.* **2019**, *4*, 1336−1341.

(12) Tao, H.; Choi, C.; Ding, L. X.; Jiang, Z.; Han, Z.; Jia, M.; Fan, Q.; Gao, Y.; Wang, H.; Robertson, A. W.; Hong, S.; Jung, Y.; Liu, S.; Sun, Z. Nitrogen fixation by Ru single-atom electrocatalytic reduction. *Chem* **2019**, *5*, 204−214.

(13) Yu, B.; Li, H.; White, J.; Donne, S.; Yi, J.; Xi, S.; Fu, Y.; Henkelman, G.; Yu, H.; Chen, Z.; et al. Tuning the catalytic preference of ruthenium catalysts for nitrogen reduction by atomic dispersion. *Adv. Funct. Mater.* **2020**, *30*, 1905665.

(14) Geng, Z.; Liu, Y.; Kong, X.; Li, P.; Li, K.; Liu, Z.; Du, J.; Shu, M.; Si, R.; Zeng, J. Achieving a record-high yield rate of 120.9 μg_{NH3} $mg^{-1}_{cat.}$ h^{-1} for N_2 electrochemical reduction over Ru single-atom catalysts. *Adv. Mater.* **2018**, *30*, 1803498.

(15) Suryanto, B. H. R.; Wang, D.; Azofra, L. M.; Harb, M.; Cavallo, L.; Jalili, R.; Mitchell, D. R. G.; Chatti, M.; MacFarlane, D. R. MoS_2 polymorphic engineering enhances selectivity in the electrochemical reduction of nitrogen to ammonia. *ACS Energy Lett.* **2019**, *4*, 430−435.

(16) Jiang, M.; Tao, A.; Hu, Y.; Wang, L.; Zhang, K.; Song, X.; Yan, W.; Tie, Z.; Jin, Z. Crystalline modulation engineering of Ru nanoclusters for boosting ammonia electrosynthesis from dinitrogen or nitrate. *ACS Appl. Mater. Interfaces* **2022**, *14*, 17470−17478.

(17) Shi, M. M.; Bao, D.; Wulan, B. R.; Li, Y. H.; Zhang, Y. F.; Yan, J. M.; Jiang, Q. Au sub-nanoclusters on TiO_2 toward highly efficient and selective electrocatalyst for N_2 conversion to NH_3 at ambient conditions. *Adv. Mater.* **2017**, *29*, 1606550.

(18) Nash, J.; Yang, X.; Anibal, J.; Wang, J.; Yan, Y.; Xu, B. Electrochemical nitrogen reduction reaction on noble metal catalysts in proton and hydroxide exchange membrane electrolyzers. *J. Electrochem. Soc.* **2017**, *164*, F1712−F1716.

(19) Wang, J., Yu, L., Hu, L., Chen, G., Xin, H., Feng, X. Ambient ammonia synthesis via palladium-catalyzed electrohydrogenation of dinitrogen at low overpotential. *Nat. Commun.* **2018**, *9*, 1795.

(20) Yang, D.; Chen, T.; Wang, Z. Electrochemical reduction of aqueous nitrogen (N_2) at a low overpotential on (110)-oriented Mo nanofilm. *J. Mater. Chem. A* **2017**, *5*, 18967−18971.

(21) Hu, L.; Khaniya, A.; Wang, J.; Chen, G.; Kaden, W. E.; Feng, X. Ambient electrochemical ammonia synthesis with high selectivity on Fe/Fe oxide catalyst. *ACS Catal.* **2018**, *8*, 9312−9319.

(22) Li, L.; Tang, C.; Xia, B.; Jin, H.; Zheng, Y.; Qiao, S. Z. Two-dimensional mosaic bismuth nanosheets for highly selective ambient electrocatalytic nitrogen reduction. *ACS Catal.* **2019**, *9*, 2902−2908.

(23) Lu, K.; Xia, F.; Li, B.; Liu, Y.; Abdul Razak, I. B.; Gao, S.; Kaelin, J.; Brown, D. E.; Cheng, Y. Synergistic multisites $Fe_2Mo_6S_8$ electrocatalysts for ambient nitrogen conversion to ammonia. *ACS Nano* **2021**, *15*, 16887−16895.

(24) Yang, X.; Nash, J.; Anibal, J.; Dunwell, M.; Kattel, S.; Stavitski, E.; Attenkofer, K.; Chen, J. G.; Yan, Y.; Xu, B. Mechanistic insights into electrochemical nitrogen reduction reaction on vanadium nitride nanoparticles. *J. Am. Chem. Soc.* **2018**, *140*, 13387−13391.

(25) Jin, H.; Li, L.; Liu, X.; Tang, C.; Xu, W.; Chen, S.; Song, L.; Zheng, Y.; Qiao, S. Z. Nitrogen vacancies on 2D layered W_2N_3: A stable and efficient active site for nitrogen reduction reaction. *Adv. Mater.* **2019**, *31*, 1902709.

(26) Song, Y.; Johnson, D.; Peng, R.; Hensley, D. K.; Bonnesen, P. V.; Liang, L.; Huang, J.; Yang, F.; Zhang, F.; Qiao, R.; et al. A physical catalyst for the electrolysis of nitrogen to ammonia. *Sci. Adv.* **2018**, *4*, e1700336.

(27) Mukherjee, S.; Cullen, D. A.; Karakalos, S.; Liu, K.; Zhang, H.; Zhao, S.; Xu, H.; More, K. L.; Wang, G.; Wu, G. Metal-organic framework-derived nitrogen-doped highly disordered carbon for electrochemical ammonia synthesis using N_2 and H_2O in alkaline electrolytes. *Nano Energy* **2018**, *48*, 217−226.
(28) Lazouski, N.; Schiffer, Z. J.; Williams, K.; Manthiram, K. Understanding continuous lithium-mediated electrochemical nitrogen reduction. *Joule* **2019**, *3*, 1127−1139.
(29) Li, K.; Andersen, S. Z.; Statt, M. J.; Saccoccio, M.; Bukas, V. J.; Krempl, K.; Sažinas, R.; Pedersen, J. B.; Shadravan, V.; Zhou, Y.; et al. Enhancement of lithium-mediated ammonia synthesis by addition of oxygen. *Science* **2021**, *374*, 1593−1597.
(30) Searle, P. L. The Berthelot or indophenol reaction and its use in the analytical chemistry of nitrogen. *Analyst* **1984**, *109*, 549−568.
(31) Li, L.; Tang, C.; Yao, D.; Zheng, Y.; Qiao, S. Z. Electrochemical nitrogen reduction: Identification and elimination of contamination in electrolyte. *ACS Energy Lett.* **2019**, *4*, 2111−2116.
(32) Kibsgaard, J.; Nørskov, J. K.; Chorkendorff, I. The difficulty of proving electrochemical ammonia synthesis. *ACS Energy Lett.* **2019**, *4*, 2986−2988.
(33) Chen, Y.; Liu, H.; Ha, N.; Licht, S.; Gu, S.; Li, W. Revealing nitrogen-containing species in commercial catalysts used for ammonia electrosynthesis. *Nat. Catal.* **2020**, *3*, 1055−1061.
(34) Greenlee, L. F.; Renner, J. N.; Foster, S. L. The use of controls for consistent and accurate measurements of electrocatalytic ammonia synthesis from dinitrogen. *ACS Catal.* **2018**, *8*, 7820−7827.
(35) Andersen, S. Z.; Čolić, V.; Yang, S.; Schwalbe, J. A.; Nielander, A. C.; McEnaney, J. M.; Enemark-Rasmussen, K.; Baker, J. G.; Singh, A. R.; Rohr, B. A.; et al. A rigorous electrochemical ammonia synthesis protocol with quantitative isotope measurements. *Nature* **2019**, *570*, 504−508.
(36) Suryanto, B. H.; Du, H. L.; Wang, D.; Chen, J.; Simonov, A. N.; MacFarlane, D. R. Challenges and prospects in the catalysis of electroreduction of nitrogen to ammonia. *Nat. Catal.* **2019**, *2*, 290−296.
(37) Tang, C.; Qiao, S. Z. How to explore ambient electrocatalytic nitrogen reduction reliably and insightfully. *Chem. Soc. Rev.* **2019**, *48*, 3166−3180.
(38) Choi, J.; Suryanto, B. H. R.; Wang, D.; Du, H. L.; Hodgetts, R. Y.; Ferrero Vallana, F. M.; MacFarlane, D. R.; Simonov, A. N. Identification and elimination of false positives in electrochemical nitrogen reduction studies. *Nat. Commun.* **2020**, *11*, 5546.
(39) Hu, L.; Xing, Z.; Feng, X. Understanding the electrocatalytic interface for ambient ammonia synthesis. *ACS Energy Lett.* **2020**, *5*, 430−436.

(40) Gao, D.; Zhou, H.; Wang, J.; Miao, S.; Yang, F.; Wang, G.; Wang, J.; Bao, X. Size-dependent electrocatalytic reduction of CO_2 over Pd nanoparticles. *J. Am. Chem. Soc.* **2015**, *137*, 4288−4291.

(41) Wu, L.; Ji, Y.; Dai, D.; Chen, T.; Yang, D.; Liu, Y.; Wang, Z. Exceptional size-dependent activity enhancement in the catalytic electroreduction of N_2 over Mo nanoparticles. *Int. J. Hydrogen Energy* **2020**, *45*, 31841−31848.

(42) Fiévet, F.; Ammar-Merah, S.; Brayner, R.; Chau, F.; Giraud, M.; Mammeri, F.; Peron, J.; Piquemal, J. Y.; Sicard, L.; Viau, G. The polyol process: a unique method for easy access to metal nanoparticles with tailored sizes, shapes and compositions. *Chem. Soc. Rev.* **2018**, *47*, 5187−5233.

(43) Zawadzki, M.; Okal, J. Synthesis and structure characterization of Ru nanoparticles stabilized by PVP or γ-Al_2O_3. *Mater. Res. Bull.* **2008**, *43*, 3111−3121.

(44) Su, N.; Gao, X.; Chen, X.; Yue, B.; He, H. The enantioselective hydrogenation of acetophenone over Pd concave tetrahedron nanocrystals affected by the residual adsorbed capping agent polyvinylpyrrolidone (PVP). *J. Catal.* **2018**, *367*, 244−251.

(45) Gao, Z.; Le, D.; Khaniya, A.; Dezelah, C. L.; Woodruff, J.; Kanjolia, R. K.; Kaden, W. E.; Rahman, T. S.; Banerjee, P. Self-catalyzed, low-temperature atomic layer deposition of ruthenium metal using zero-valent Ru(DMBD)$(CO)_3$ and water. *Chem. Mater.* **2019**, *31*, 1304−1317.

(46) Green, C. L.; Kucernak, A. Determination of the platinum and ruthenium surface areas in platinum−ruthenium alloy electrocatalysts by underpotential deposition of copper. I. Unsupported catalysts. *J. Phys. Chem. B* **2002**, *106*, 1036−1047.

(47) Chen, G. F.; Cao, X.; Wu, S.; Zeng, X.; Ding, L. X.; Zhu, M.; Wang, H. Ammonia electrosynthesis with high selectivity under ambient conditions via a Li^+ incorporation strategy. *J. Am. Chem. Soc.* **2017**, *139*, 9771−9774.

(48) Watt, G. W.; Chrisp, J. D. A spectrophotometric method for the determination of hydrazine. *Anal. Chem.* **1952**, *24*, 2006−2008.

(49) Cotton, F. A.; Wilkinson, G.; Murillo, C. A.; Bochmann, M. *Advanced Inorganic Chemistry*, 6th ed.; Wiley: New York, 1999.

(50) García-Robledo, E.; Corzo, A.; Papaspyrou, S. A fast and direct spectrophotometric method for the sequential determination of nitrate and nitrite at low concentrations in small volumes. *Mar. Chem.* **2014**, *162*, 30−36.

(51) Li, J.; Zhan, G.; Yang, J.; Quan, F.; Mao, C.; Liu, Y.; Wang, B.; Lei, F.; Li, L.; Chan, A. W. M.; et al. Efficient ammonia electrosynthesis from nitrate on strained ruthenium nanoclusters. *J. Am. Chem. Soc.* **2020**, *142*, 7036−7046.

(52) Gavnholt, J.; Schiøtz, J. Structure and reactivity of ruthenium nanoparticles. *Phys. Rev. B* **2008**, *77*, 035404.

(53) Skulason, E.; Bligaard, T.; Gudmundsdóttir, S.; Studt, F.; Rossmeisl, J.; Abild-Pedersen, F.; Vegge, T.; Jonsson, H.; Nørskov, J. K. A theoretical evaluation of possible transition metal electro-catalysts for N_2 reduction. *Phys. Chem. Chem. Phys.* **2012**, *14*, 1235−1245.
(54) Tayyebi, E.; Abghoui, Y.; Skulason, E. Elucidating the mechanism of electrochemical N_2 reduction at the Ru(0001) electrode. *ACS Catal.* **2019**, *9*, 11137−11145.
(55) Zhao, X.; Liu, Y. Origin of selective production of hydrogen peroxide by electrochemical oxygen reduction. *J. Am. Chem. Soc.* **2021**, *143*, 9423−9428.
(56) Chan, K.; Nørskov, J. K. Electrochemical barriers made simple. *J. Phys. Chem. Lett.* **2015**, *6*, 2663−2668.
(57) Huang, Y.; Nielsen, R. J.; Goddard III, W. A. Reaction mechanism for the hydrogen evolution reaction on the basal plane sulfur vacancy site of MoS_2 using grand canonical potential kinetics. *J. Am. Chem. Soc.* **2018**, *140*, 16773−16782.
(58) Lindgren, P.; Kastlunger, G.; Peterson, A. A. A challenge to the $G\sim0$ interpretation of hydrogen evolution. *ACS Catal.* **2020**, *10*, 121−128.